Patient-specific compliant simulation framework informed by 4DMRI-extracted Pulse Wave Velocity: Application post-TEVAR

Louis Girardin[a,b,1], Niklas Lind[c,2], Hendrik von Tengg-Kobligk[c,3], Stavroula Balabani[a,b,4],Vanessa Díaz-Zuccarini[a,b,5]

a University College London, Department of Mechanical Engineering, Torrington Place, London WC1E7JE, UK

b Welcome/ESPRC Centre for Interventional and Surgical Sciences (WEISS), 43-45 Foley Street, London W1W7TS, UK

c Department of Diagnostic of Interventional and Pediatric Radiology, Inselspital, Bern 3010, Switzerland

[1] ucemgir@ucl.ac.uk

[2] niklas.lind@extern.insel.ch

[3] hendrik.vontengg@insel.ch

[4] s.balabani@ucl.ac.uk

[5] v.diaz@ucl.ac.uk

Abstract

We introduce a new computational framework that makes use of the Pulse Wave Velocity (PWV) extracted exclusively from 4D flow MRI (4DMRI) to inform patient-specific compliant computational fluid dynamics (CFD) simulations of a Type-B aortic dissection (TBAD), post-thoracic endovascular aortic repair (TEVAR). From 4DMRI and brachial pressure, a 3D inlet velocity profile (IVP), dynamic outlet boundary, and reconstructed thoracic aortic geometry are obtained. A moving boundary method (MBM) is applied to simulate aortic wall displacement. The aortic wall stiffness was estimated through two methods: one relying on area-based distensibility and the other utilising regional pulse wave velocity (RPWV) distensibility, further fine-tuned to align with *in vivo* values. Predicted pressures and outlet flow rates were within 2.3% of target values. RPWV-based simulations were more accurate in replicating *in vivo* hemodynamic compared to the area-based ones. RPWVs were closely predicted in most regions, with the exception being the endograft, and systolic flow reversal ratios (SFRR) were accurately captured, while a difference of above 60% on in-plane rotational flow (IRF) between the simulations. Significant disparities between the wall shear stress (WSS)-based indices were observed between the two approaches, especially the endothelial cell activation potential (ECAP). At the isthmus, the RPWV-driven simulation indicated a mean ECAP>$1.4Pa^{-1}$ (critical threshold), indicating areas potentially prone to thrombosis. In contrast, the area-based simulation did not depict this. RPWV-driven simulation results agree well with 4DMRI measurements, emphasising that RPWV simulations are accurate in simulating haemodynamics, consequently facilitating a comprehensive assessment of surgery decision-making and potential complications, such as thrombosis and aortic growth.

Keywords: CFD, Type-B Aortic Dissection, Pulse Wave Velocity, 4DMRI, Compliant Simulation

1. Introduction

Type-B Aortic Dissection (TBAD) affects 3 in 100,000 people annually (Trahanas et al., 2022).Surgical intervention is necessary when complications like aneurysmal dilatation arise. TBAD open surgery carries high mortality rates, about 20% (Yuan et al., 2018). In recent decades, thoracic endovascular aortic repair (TEVAR) has emerged as a less invasive surgical approach with favourable post-operative survival rates (Jiang et al., 2023). TEVAR is an endovascular surgery which aims to restore normal aortic function by covering the initial entry tear and promoting thrombosis of the false lumen (Uchida and Sadahiro, 2018). While various studies have highlighted TEVAR advantages (Nienaber et al., 2013; Singh et al., 2021; Tadros et al., 2019), TEVAR remains associated with outcomes such as endoleaks and high mortality rates (Bavaria et al., 2022). TEVAR for TBAD requires follow-up screenings to prevent and predict complications (Eidt and Vasquez, 2023; Williams et al., 2022).

Elevated pulse wave velocity (PWV) is associated with aortic stiffening and TEVAR, as the endograft rigidifies the aorta (De Beaufort et al., 2017; Hori et al., 2020). Increasing PWV has been linked with cardiovascular outcomes such as stroke and left ventricular hypertrophy (Valencia-Hernández et al., 2022). PWV can be determined through 2D flow MRI or cine-MRI by assessing the pulse wave travel time along the aortic centerline or the distensibility by measuring the cross-sectional variations of the vessel throughout the cardiac cycle (Wentland et al., 2014). The regional PWV (RPWV) can be measured on 4DMRI, providing the local stiffness of the vessel (Nguyen et al., 2023; Wentland et al., 2014). RPWV is significant in the context of TEVAR due to the proximal aortic stiffening after the endograft placement (Bissacco et al., 2022).

TEVAR can induce aortic wall remodelling and abnormal flow, affecting wall shear stress (WSS) (Midulla et al., 2021), possibly leading to endothelial dysfunction with outcomes such as thrombosis (Morbiducci et al., 2009; Nauta et al., 2017). 4DMRI allows the assessment of various functional parameters, such as blood flow dynamics, which is not conventionally measured in the clinical assessment of TEVAR (Cosset et al., 2022; Takahashi et al., 2022). However, its low near-wall spatial resolution limits the quantification of pressure and WSS in abnormal regions (Lamata et al., 2014; Markl et al., 2011). Computational fluid dynamics (CFD) simulations can be fused with 4DMRI to calculate these haemodynamic variables accurately (Armour et al., 2022; Black et al., 2023).

CFD simulations are beneficial in the context of TEVAR to assess the impact of compliance mismatch introduced by endografts. Fluid-structure interaction (FSI) has traditionally been used for patient-specific simulations of TEVAR procedures, for example, to study their impact on cardiac remodelling and left ventricular afterload (Van Bakel et al., 2019) or the flow reversal due to the rigidity and length of the endograft (Aghilinejad et al., 2022) and their impact on left ventricular afterload. However, FSI is computationally costly and often based on literature values of elastic or anisotropic tissue data, as *in vivo* data are barely accessible (Wang et al., 2023) or impossible to obtain. To circumvent these challenges, different alternatives have been developed. Recently, a mesh morphing technique based on dynamic CT imaging was proposed to allow the reconstruction of the transient aortic geometry(Capellini et al., 2021, 2018). The technique was used to study large-scale flow coherence in ascending aorta(Calò et al., 2023). A moving boundary method (MBM) was developed, in-house, as a less-costly alternative based on a non-imposed radial nodal displacement calculation and has been applied in several studies (Bonfanti et al., 2018, 2017; Girardin et al., 2024; Stokes et al., 2021).

In this study, a 4DMRI-informed computational method based on our MBM is developed, using 4D flow MR and non-invasive pressure measurements to inform patient-specific, compliant CFD simulations of TBAD post-TEVAR. More specifically, RPWVs, a routinely used clinical marker, are extracted from 4DMRI using a cross-correlation method to tune iteratively the aortic stiffness used in the simulations. Additional simulations with stiffness derived from the area-based distensibility are conducted. Hemodynamic indices are estimated and compared.

2. Methods

2.1. Data Acquisition

A patient with chronic TBAD previously treated with TEVAR was presented for follow-up at Inselspital Bern. Their aorta was imaged following an ethically approved protocol (Local Institutional Review Board ID 2019-00556). MRI sequences of the thoracic aorta down to the abdominal aorta were acquired using a MAGNETOM Sola fit scanner (Siemens Healthineers). 4DMRI was acquired with a resolution of 2.5 mm*2.5 mm*2.5 mm. A T2/T1 weighted TRUFI MRI sequence was acquired with a 1 mm*1 mm* 1 mm resolution. Cine-MRI and 2D flow MRI (2DMRI) were acquired with a resolution of 1.875 mm*1.875 mm. Brachial pressure was acquired before the examinations.

2.2. Segmentations and Meshing

The aorta was segmented from the T2/T1 TRUFI using ScanIP (Synopsis Simpleware, USA). The combined geometry was smoothed using MeshMixer (Autodesk, USA). Inlet and outlets were trimmed perpendicularly to their cross-sectional area using Fluent Mesh (Ansys Fluent, USA) (Fig 1a). The geometry was separated into discrete regions along the centreline based on anatomical and stiffness characteristics observed with the wall displacement features on the 4DMRI (Fig 1).
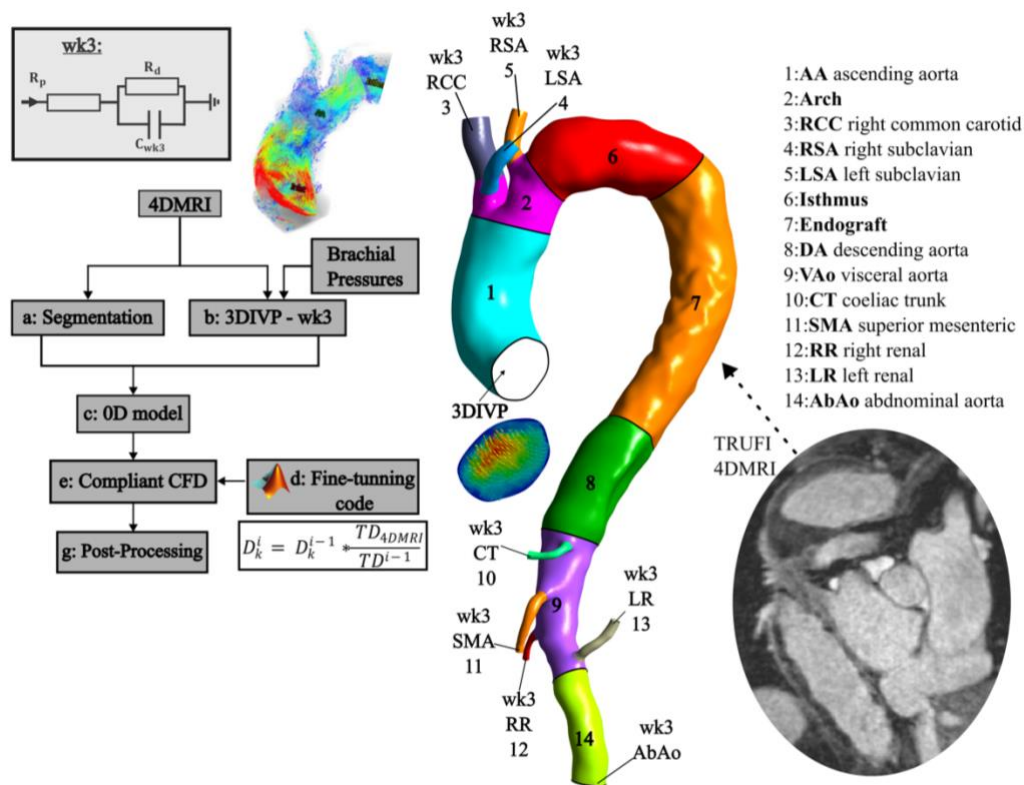
[Fig 1 about here]

Fig 1 Process diagram showing the calibration steps (a-g) for the patient-specific compliant simulation, informed via RPWVs.

A tetrahedral computational mesh was created using the segmented geometry with Fluent Mesh 19.0 (Ansys Inc., USA). Details on the mesh element sizing, parameters used for the prism layering, and the mesh sensitivity analysis used to obtain the final mesh are available in Appendix 1.

2.3. Boundary Conditions

Following our previous work (Stokes et al., 2023b), 4DMRI was used to extract a 3D inlet velocity profile (3DIVP) and outlet mean flow rates (Fig. 1a) using GTFlow (GyroTools LLC, Switzerland) (Table 1). The 3DIVP was spline-interpolated to apply a 1ms CFD timestep using MATLAB (MathWorks Inc., USA) (Fig. 1b).

Table 1 Target mean flow rates at outflow boundaries and inlet systolic and diastolic pressures against CFD values.

	Flow rate [mL/s]								Pressure [mmHg]	
	RCC	RSA	LCC	CT	SMA	LR	RR	AbAo	Systole	Diastole
Target	18.88	7.41	8.12	3.13	8.25	1.87	1.50	14.70	101.8	70
S1	18.98	7.38	8.09	3.17	8.21	1.89	1.50	14.63	100.36	68.4
S2	18.75	7.35	8.15	3.12	8.33	1.84	1.53	14.75	102.5	70.5

4

A 0D lumped parameter model of the vasculature (20-sim, Controllab Products, Netherlands) was used to calibrate three-element Windkessel (WK3) parameters (Fig 1c), used at the outlets as pressure boundary conditions in the CFD as described in previous works (Stokes et al., 2023b; Westerhof et al., 2009). Parameter values are displayed in Appendix 2.

2.4. Moving Boundary Method & Stiffness Tuning

The MBM introduced by (Bonfanti et al., 2018)was used to simulate the compliant behaviour of the aorta. According to this method, the local wall displacement follows the surface node normal, proportional to the difference between nodal pressure and exterior pressure and the local wall stiffness. The stiffness K_i (N/m^3) is equal to:

$$K_i = \frac{2}{D_k}\sqrt{\frac{\pi}{A_0}}$$

(1)

where A_0 (m^2) is the local cross-sectional area at diastole, and D_k (1/Pa) is the local wall distensibility. Local stiffness values (K_i) were initially calculated using a distensibility D_k defined by the ratio between the cross-sectional relative change, as measured by the 4DMR images, and the regional pulse pressure, such as:

$$D_k = \frac{A_{max,k} - A_{min,k}}{A_{min,k}\Delta p_k}$$

(2)

where $A_{max,k}$ and $A_{min,k}$ (m^2) are the maximum and minimum cross-sectional area of the aortic vessel in a region k and Δp_k is the pulse pressure in the region k, estimated through transient CFD simulations assuming a rigid wall. When no displacements could be extracted from 4DMRI due to its spatial resolution, the distensibility was estimated from the RPWV using the empirical relationship from (Reymond et al., 2009):

$$D_k = \rho^{-1}RPWV_k^{-2}$$

(3)

Where ρ is the density of blood (kg/m^3). RPWVs were estimated from the 4DMRI in each region using a cross-correlation method (Fielden et al., 2008; Markl et al., 2010), as illustrated in Fig. 2.
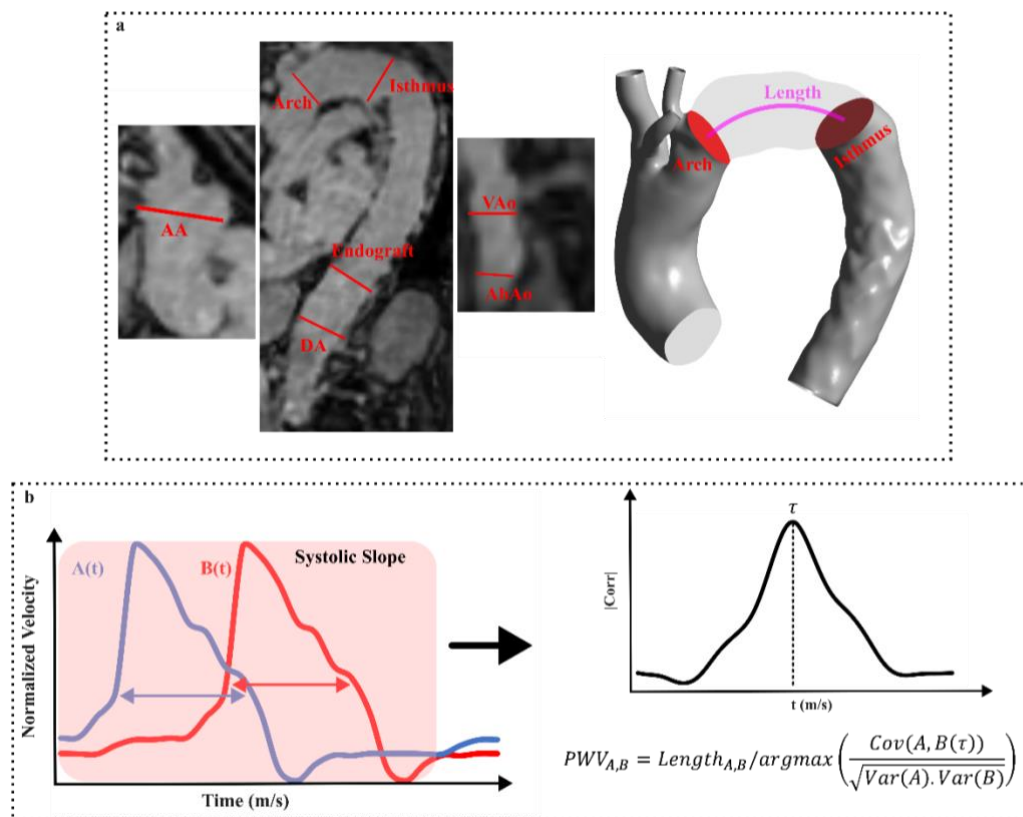

$$PWV_{A,B} = Length_{A,B}/argmax\left(\frac{Cov(A,B(\tau))}{\sqrt{Var(A).Var(B)}}\right)$$

Fig 2 a.- Red lines depict the 4DRMI planes on which the flow rates were measured. b.- schematic of the cross-correlation method used to calculate the PWV between planes A and B.

In the endograft region, this method yielded a distensibility of $1.6 * 10^{-3} mmHg^{-1}$, which is an order of magnitude higher than reported values in the literature (Johnston et al., 2010; Rovas et al., 2023; Tremblay et al., 2009). Considering the possibility of measurement noise proximal to the endograft, we opted to use a literature-based distensibility value of $1.6 * 10^{-4} mmHg^{-1}$ in the calculation of stiffness in this region.

A varying, patient-specific stiffness field was thus calculated using RPWV-based distensibility. An automatic iterative method was developed to tune the stiffness field to match the 4DMRI RPWVs and exemplified in Fig. 1. A MATLAB code calls CFX (Ansys Inc., USA) and updates the simulation script with a new stiffness in each run. Only the systolic phase was run to avoid potential wave reflection during diastole and to reduce the computational time of the iterative process. At the end of each run, flow rates were extracted from the planes enclosing the regions of interest and the RPWVs were calculated (Fig 2). The distensibility of each region k, D_k (1/Pa), was then updated following the equation below:

$$D_k^i = D_k^{i-1} * \frac{TD_{4DMRI}}{TD^{i-1}} \tag{4}$$

The process was run until the time delay error was lower than 10%; seven iterations were required, each taking 3 hours in an 8 Intel Core i9-11900K. The final stiffness map was inputted to the full simulation (Fig 3). S1 denotes simulations obtained with the stiffness map extracted from the area changes (equations 1 and 2), and S2 is the one based on RPWV estimates, using equations 1 and 4.
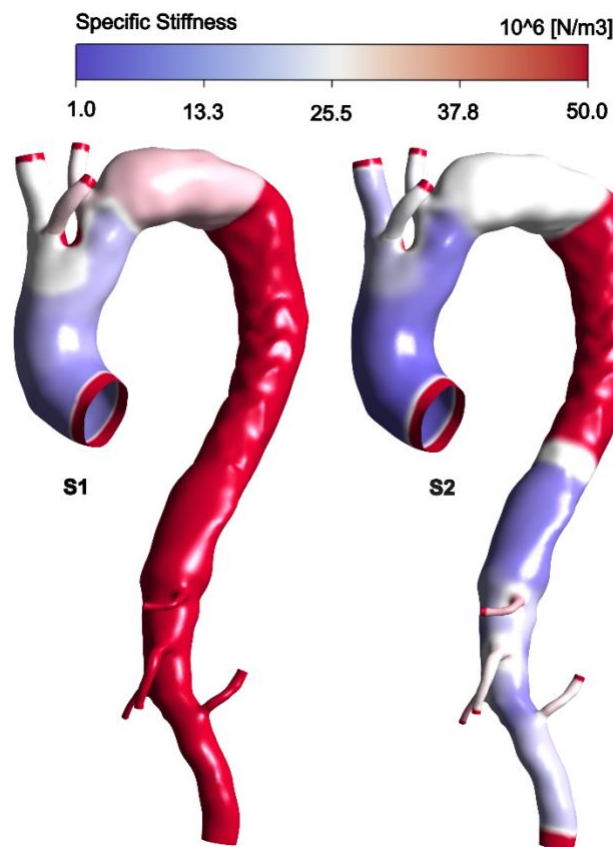

Fig 3 Stiffness maps produced from area- and RPWV-based distensibility used to compare S1 and S2 with a logarithmic scale, respectively.

2.5. Simulation Model

The finite-volume solver ANSYS CFX 19.0 was employed to solve the transient three-dimensional Navier-Stokes equations (Fig . 1d,e). These equations considered the Carreau-Yasuda viscosity model and used empirical constants derived from the work of (Tomaiuolo et al., 2016). Blood was modelled as incompressible and non-Newtonian, with a 1056 kg/m³ density. The peak Re_p and critical Re_c Reynolds numbers computed as in (Peacock et al., 1998), were equal to 6855 and 6000, respectively. Therefore, the k-ω shear stress transport model was employed to model the turbulence with a low turbulence intensity of 1% introduced to the flow (Kousera et al., 2013). The Navier-Stokes and continuity equations were solved with a second-order backward Euler scheme, using a 1ms time step. The convergence criterion was set to a root-mean-square residual value of 10^{-5} for all equations within each time step. A state of periodicity characterised by less than 1% variation in systolic and

diastolic pressures between cycles (Fig. 1d,g) was reached after four cycles for both simulations, and the results of the last cycle were post-processed to extract the hemodynamic indices reported below.

3. Results

3.1. Validation

Mean flow rates and diastolic and systolic pressures are shown against target values in Table 1. S1 and S2 pressures and mean flow rates at flow boundaries were predicted within 2.3% of error.

The simulated RPWVs were compared against the 4DMRI ones in the regions of interest (Fig 4). Results show that S1 systematically overestimates PWV due to the high stiffness values across most of the flow domain, starting from the isthmus to the AbAo (Fig 3). In S2, a maximum error of 8% was found in the arch and DA regions except the endograft; this corresponds to a 1 ms difference in travel time.
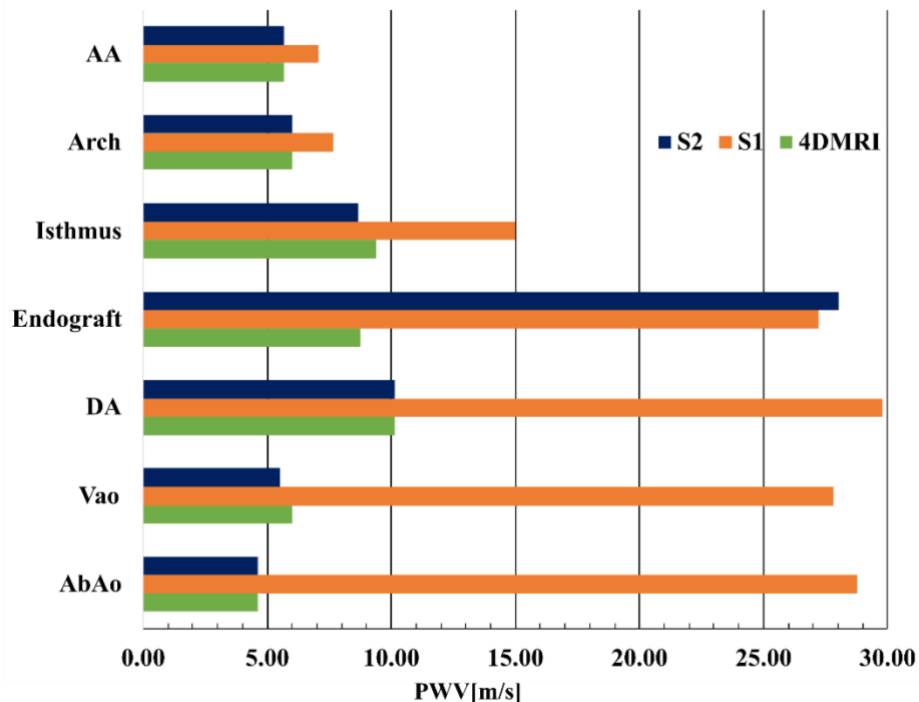

Fig 4 Comparison of predicted RPWVs, S1 (orange) and S2 (green), against 4DMRI extracted (blue).

3.2. Flow characteristics

The systolic flow reversal ratio (SFRR), the ratio between backward and forward flow during systole, is a clinical marker linked with local dilation when increasing (Gil-Sala et al., 2021). SFRR was evaluated across the planes enclosing the regions of interest shown in Fig 1a. 4DMRI estimated SFRR values exceeded 30% in the AA region (Fig 5), which can be attributed to the circulating flow pattern at the inlet. Moreover, the stenosis at the arch causes upstream flow acceleration and recirculation and a build-up of pressure before the stenosis, leading to about half of the flow going backwards during systole. The compliance mismatch between the proximal aortic aorta and the endograft can lead to a pronounced SFRR (Sultan et al., 2021). In our study, an SFRR >30% at the interface between the isthmus and the DA with the endograft is consistent with these reported findings. Downstream of the endograft, where the compliance mismatch is less pronounced and the geometry more tubular and straight, the SFRR decreases to 18% and 14% at the VAo and AbAo, respectively. The maximum difference between the 4DMRI and the predicted SFRR in S1 occurred at the DA.
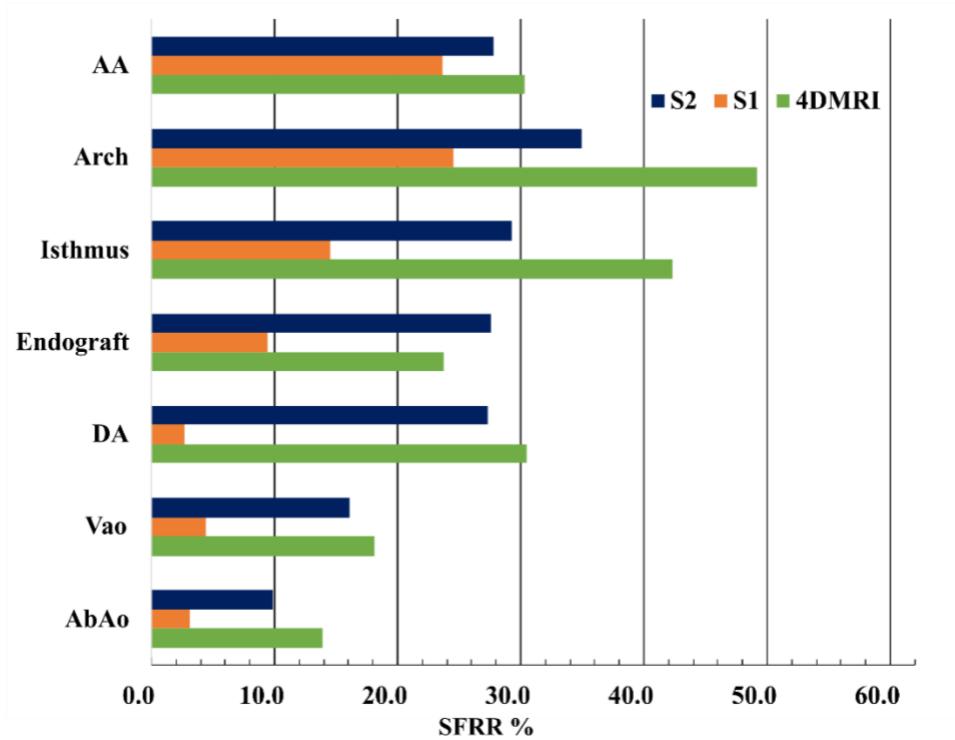
7

Fig 5 Comparison between 4DMRI (blue) measured and predicted -, S1 (orange) and S2 (green)-SFRR values along the aortic domain.

Previous research showed the reduction of the in-plane rotational flow (IRF) in rigidified and dilated aortae, which are correlated outcomes of TBAD and TEVAR (Dux-Santoy et al., 2019; Gil-Sala et al., 2021). IRF is not presented for the 4DMRI due to the spatial resolution limitations, resulting in inaccurate calculations of the finite differences used to evaluate the vorticity. Similarly to the flow reversal trends, S1 appear to overpredict IRF compared to S2, particularly in regions with significant stiffness differences between the two simulations, such as at the isthmus, DA, VAo and AbAo, with differences exceeding 60% (Fig. 6).
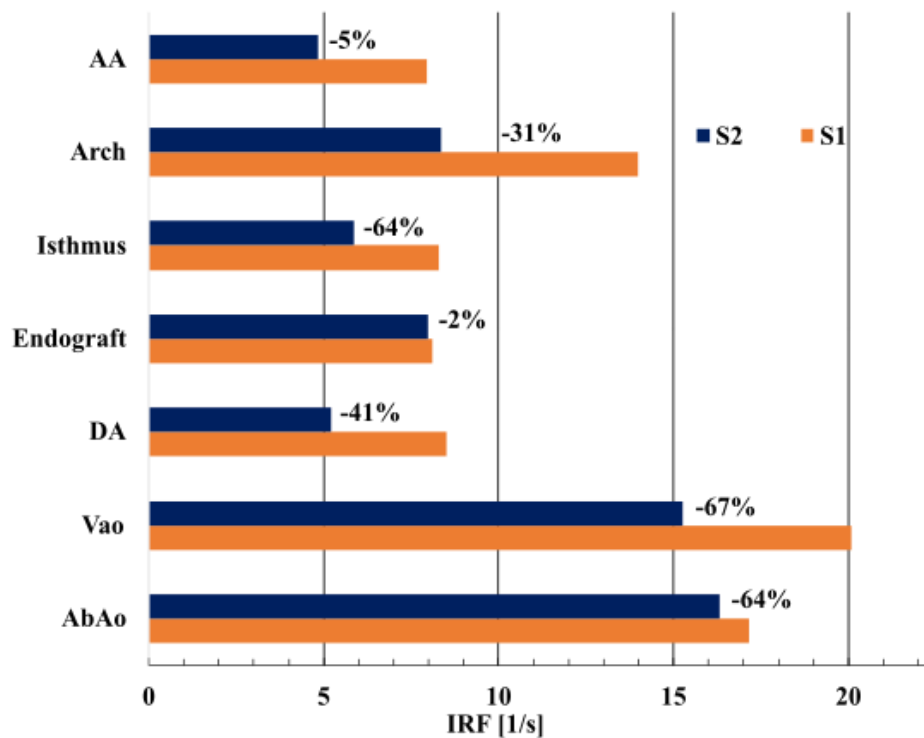

Fig 6 IRF for S1 (blue) and S2 (orange) with the difference reported next to the bar.

8

Velocity magnitude contours at different flow phases and on selected planes are shown in Fig. 7. S2 demonstrates a better qualitative agreement with the 4DMRI, capturing velocity magnitude distribution more accurately, such as at T1 and T3 on ii. The peak velocity displacement is also better reproduced in S2, such as at T3 on i and ii. A limitation observed in the 4DMRI data is the resulting coarser images at T4 during late diastole, which makes comparison with simulations difficult, and which a priori show limited agreement likely due to poor signal to noise ratio.
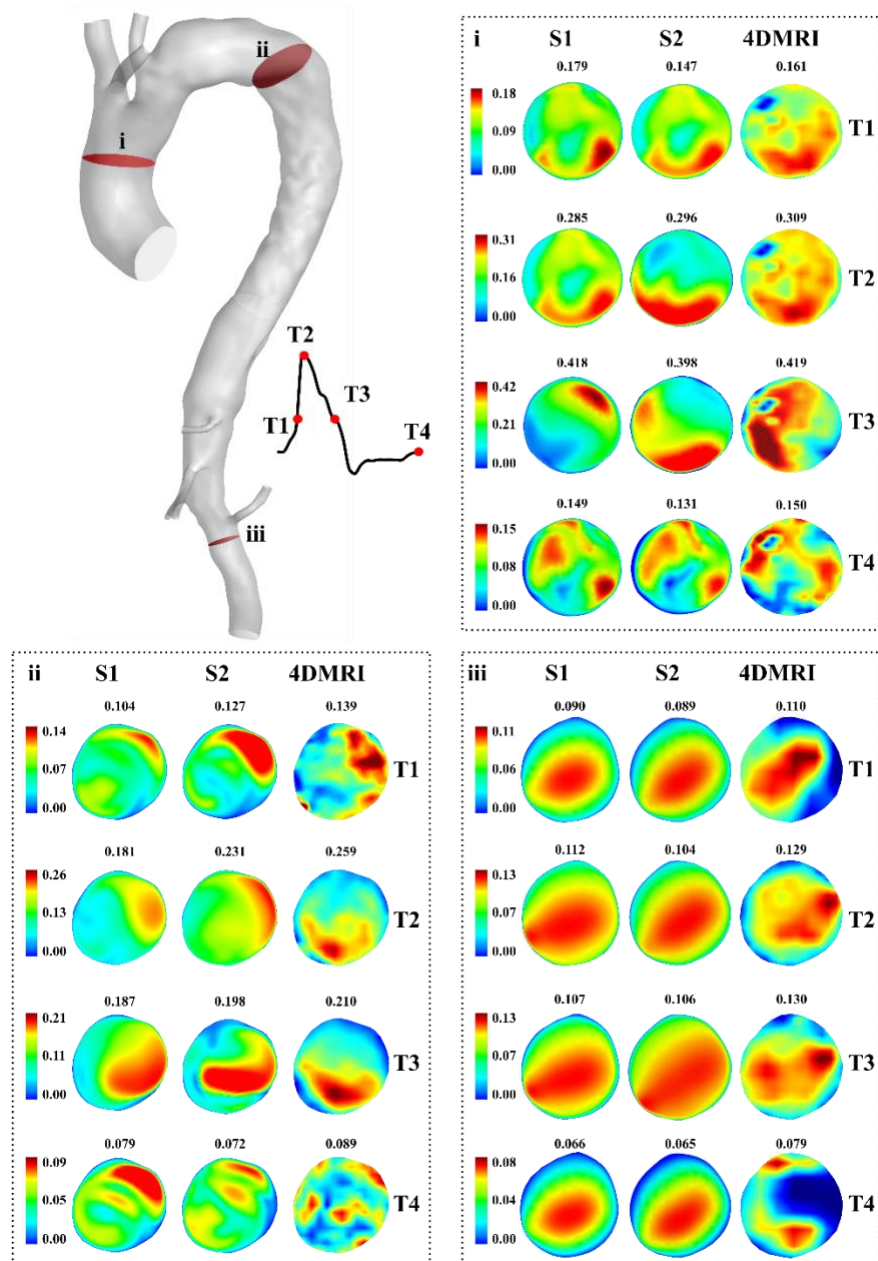

Fig 7 Contours of velocity magnitude at different flow phases in each case at the AA (i), endograft (ii) and Vao (iii).

3.3. Wall shear stress indices

Contours of time-average wall shear stress (TAWSS), oscillatory shear index (OSI) and endothelial cell activation potential (ECAP) (Di Achille et al., 2014; D. Gallo et al., 2012) predicted from the two simulation approaches and the point-wise difference between them are displayed in Fig 8. Table 2 displays the minimum, maximum and mean values on each region for S2 and the average relative error between S2 and S1 per region.

TAWSS distributions obtained with S1 and S2 are qualitatively similar. In S2, the highest TAWSS values were found at the AA, arch and especially Vao (13.35Pa), where high velocities occur (Chen et al., 2013a; Wee et al.,

9

2018). The OSI distributions differ broadly between S2 and S1, indicating mean relative errors >20% downstream of the arch, promoted by substantially different flow conditions predicted therein. Point-wise differences reach a min of -0.24 at the isthmus and a min and max of -0.22 and 0.24 at the Vao.

While qualitative agreements between simulations were observed in the ECAP distributions, notable differences in region exceeding the critical threshold of $1.4 Pa^{-1}$ (Di Achille et al., 2014) were present in the sinotubular junction, isthmus and AbAo regions (Fig 8).
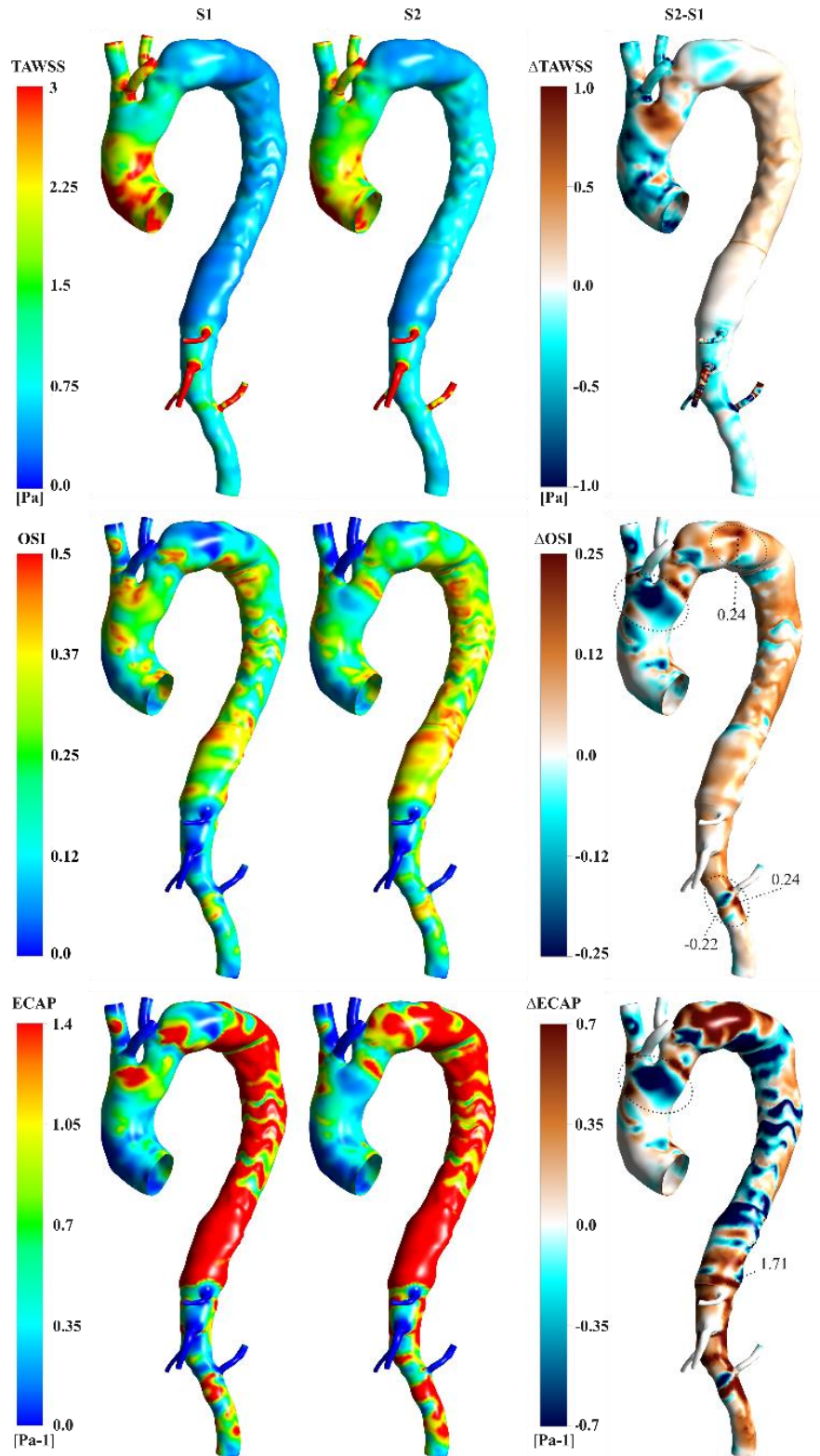
Fig 8 Contours of TAWSS, OSI, RRT and ECAP for S1 (left) and S2 (centre) and point-wise differences such as S1-S2 (right). Values on regions discussed in the core text are reported with dotted circles and lines.

		TAWSS [Pa]	OSI -	ECAP [Pa]
1:AA	Min	0.26	0.01	0.00
	Max	1.83	0.49	1.68
	Mean	1.74	0.17	0.31
	Error	1%	2%	-4%
2:Arch	Min	0.18	0.00	0.00
	Max	2.14	0.49	2.01
	Mean	0.62	0.19	0.44
	Error	15%	16%	-13%
6:Isthmus	Min	0.07	0.04	0.18
	Max	1.29	0.49	5.18
	Mean	0.25	0.28	1.88
	Error	56%	43%	44%
7:Endograft	Min	0.07	0.15	0.31
	Max	0.70	0.50	4.24
	Mean	0.26	0.34	1.40
	Error	94%	39%	-31%
8:DA	Min	0.08	0.04	0.07
	Max	0.50	0.50	5.13
	Mean	0.17	0.37	2.35
	Error	10%	33%	-17%
9:Vao	Min	0.09	0.00	0.00
	Max	13.35	0.49	3.77
	Mean	0.56	0.14	0.65
	Error	1%	29%	12%
14:AbAo	Min	0.12	0.01	0.04
	Max	0.43	0.47	3.05
	Mean	0.23	0.21	0.96
	Error	30%	21%	13%

Table 2 Minimum, maximum and mean values per region for S2. Also shown are mean relative errors value such as $Error = \left(\frac{metric_{S2} - metric_{S1}}{mmetric_{S1}} \right)$.

4. Discussion

We present a novel simulation framework driven by a single image modality (4DMRI) and informed by routinely used PWV measurements applied to a patient-specific, compliant CFD simulation of TBAD after TEVAR. Two simulation approaches were compared, differing in how the local wall stiffness informing the MBM is calculated: RPWV-based (S2) and area-based (S1). Comparing S1 and S2 simulation results highlighted that it is possible to obtain very good agreement with clinical measurements when using the RPWV-based distensibility approach whilst showing that relying solely on the area-based distensibility may not be sufficient to accurately capture patient-specific haemodynamics.

Accurate simulation of RPWVs is crucial for evaluating the haemodynamic impact of increased aortic wall stiffness after TEVAR. In this study, aortic wall stiffness, coupled with the spatial resolution limits of 4DMRI, hinders the measurement of smaller changes in aortic luminal area. Consequently, the aortic wall was considered stiff in S1, downstream of the arch, leading to inaccuracies in simulated RPWVs (Fig 4). As explained in the results section, iterative tuning of specific stiffness in S2 successfully matched in vivo RPWVs, except for the graft. A similar iterative method was employed in a Marfan syndrome CFD study using FSI, where the Young's modulus was iteratively tuned to align the simulated PWV with 4DMRI PWV (Pons et al., 2020).

After TEVAR, a compliance mismatch is introduced between the device and the proximal aorta (Sultan et al., 2022). At the interface of the endograft, different radial displacements will occur (Cao et al., 2022), resulting in increased pressure gradient and disturbed flow dynamics. A study on flow abnormalities post-TEVAR showed an increased SFRR after the treatment (Gil-Sala et al., 2021). This is well demonstrated at the endograft-vessel interfaces where limited device dilation capacity leads to flow reversal ranges of 27-42% (Fig. 5). SFRR was substantially underpredicted in the stiff regions of S1, failing to indicate flow abnormalities.

A reduction in vorticity in the aorta has been associated with promoting aortic growth and dilation (Gallo et al., 2012; Guala et al., 2019; Stokes et al., 2023a). The IRF metric has been found to drastically reduce after TEVAR in 19 patients (Guala et al., 2020). In the present study, the IRF was overpredicted in S1 compared to S2 by up to 60%, which would indicate higher risks of rupture and would be misleading (Gil-Sala et al., 2021).

High TAWSS is triggered in regions characterised by elevated velocities and risks of local disruption (Chen et al., 2013b). Our findings revealed that the TAWSS distributions of S2 and S1 were similar. Regions of TAWSS >3Pa were found at the AA, supra-aortic and visceral branches. It is worth noting that the TAWSS distribution at the AA in S2 presents fewer regions with high values >3Pa and, thus, indicate a lower potential risk of rupture.

Collocated regions of low TAWSS and high OSI are correlated with high ECAP and aneurysmal growth (Liu et al., 2019; Zhu et al., 2021). The differences in OSI distribution observed between the simulations also led to disparities in ECAP distribution. Notably, at the isthmus, where the mean ECAP is $1.88 Pa^{-1}$ and exceeds the critical threshold for S2, when this is not depicted in S1 (Fig 8.) Such disparities have significant implications for predicting thrombosis and potential vascular growth.

Additionally, the MBM assumes a linear elastic model and does not simulate longitudinal displacements, primarily in the AA (Morrison et al., 2009). However, as observed in Fig 2, the specific stiffness was reduced at the AA to match the RPWV. This allowed the longitudinal compliance to be considered within the radial compliance range and to simulate an accurate RPWV at the AA.

The limited temporal and spatial resolutions did not allow the measurement of the RPWV in any of the branches. The specific stiffness of each branch was tuned along with the proximal region to which it is attached. This assumption did not affect the simulation, as S2 matched the RPWVs well.

The work was performed with data from a single patient to build a methodology to better simulate the *in vivo* pulse wave propagation in the aorta. Future work will include validating the methodology in a patient cohort.

5. Conclusion

This new framework, utilising 4DMRI, significantly enhanced patient-specific compliant CFD simulations of arteries and was applied to a TBAD post-TEVAR. The comparison between simulations highlighted the accuracy of RPWV-based simulation in mimicking *in vivo* haemodynamics. The compliance mismatch introduced by TEVAR was well-captured, revealing pronounced SFRR and reduced IRF at endograft interfaces. This framework provided more reliable insights into predicting potential zones of cell deposition using WSS indices, which is crucial for evaluating aortic wall degeneration risks.

This approach represents a significant advancement, as simulation using area-based distensibility significantly differs from *in vivo* 4DMRI. RPWV-based simulation ensures more accurate haemodynamic assessments post-TEVAR, offering crucial insights for informed clinical decisions and risk predictions.

Acknowledgement

Reference

Aghilinejad, A., Wei, H., Magee, G.A., Pahlevan, N.M., 2022. Model-Based Fluid-Structure Interaction Approach for Evaluation of Thoracic Endovascular Aortic Repair Endograft Length in Type B Aortic Dissection 10, 1–14. https://doi.org/10.3389/fbioe.2022.825015.

Armour, C.H., Guo, B., Saitta, S., Pirola, S., Liu, Y., Dong, Z., Xu, X.Y., 2022. Evaluation and verification of patient-specific modelling of type B aortic dissection. Comput Biol Med 140. https://doi.org/10.1016/j.compbiomed.2021.105053.

Bavaria, J.E., Brinkman, W.T., Hughes, G.C., Shah, A.S., Charlton-Ouw, K.M., Azizzadeh, A., White, R.A., 2022. Five-year outcomes of endovascular repair of complicated acute type B

aortic dissections. Journal of Thoracic and Cardiovascular Surgery 163, 539-548.e2. https://doi.org/10.1016/j.jtcvs.2020.03.162.

Bissacco, D., Conti, M., Domanin, M., Bianchi, D., Scudeller, L., Mandigers, T.J., Allievi, S., Auricchio, F., Trimarchi, S., 2022. Modifications in Aortic Stiffness After Endovascular or Open Aortic Repair: A Systematic Review and Meta-Analysis. European Journal of Vascular and Endovascular Surgery 63, 567–577. https://doi.org/10.1016/j.ejvs.2022.01.008

Black, S.M.D., Maclean, C., Hall Barrientos, P., Ritos, K., McQueen, A., Kazakidi, A., 2023. Calibration of patient-specific boundary conditions for coupled CFD models of the aorta derived from 4D Flow-MRI. Front Bioeng Biotechnol 11. https://doi.org/10.3389/fbioe.2023.1178483

Bonfanti, M., Balabani, S., Alimohammadi, M., Agu, O., Homer-Vanniasinkam, S., Díaz-Zuccarini, V., 2018. A simplified method to account for wall motion in patient-specific blood flow simulations of aortic dissection: Comparison with fluid-structure interaction. Med Eng Phys 58, 72–79. https://doi.org/10.1016/j.medengphy.2018.04.014

Bonfanti, M., Balabani, S., Greenwood, J.P., Puppala, S., Homer-Vanniasinkam, S., Diáz-Zuccarini, V., 2017. Computational tools for clinical support: A multi-scale compliant model for haemodynamic simulations in an aortic dissection based on multi-modal imaging data. J R Soc Interface 14. https://doi.org/10.1098/rsif.2017.0632

Calò, K., Capellini, K., De Nisco, G., Mazzi, V., Gasparotti, E., Gallo, D., Celi, S., Morbiducci, U., 2023. Impact of wall displacements on the large-scale flow coherence in ascending aorta. J Biomech 154. https://doi.org/10.1016/j.jbiomech.2023.111620

Cao, T., Jiang, Z., Zhao, H., Zhang, K.Q., Meng, K., 2022. Numerical simulation to study the impact of compliance mismatch between artificial and host blood vessel on hemodynamics. Med Nov Technol Devices 15. https://doi.org/10.1016/j.medntd.2022.100152

Capellini, K., Gasparotti, E., Cella, U., Costa, E., Fanni, B.M., Groth, C., Porziani, S., Biancolini, M.E., Celi, S., 2021. A novel formulation for the study of the ascending aortic fluid dynamics with in vivo data. Med Eng Phys 91, 68–78. https://doi.org/10.1016/j.medengphy.2020.09.005

Capellini, K., Vignali, E., Costa, E., Gasparotti, E., Biancolini, M.E., Landini, L., Positano, V., Celi, S., 2018. Computational Fluid Dynamic Study for aTAA Hemodynamics: An Integrated Image-Based and Radial Basis Functions Mesh Morphing Approach. J Biomech Eng 140. https://doi.org/10.1115/1.4040940

Chen, D., Müller-Eschner, M., Kotelis, D., Böckler, D., Ventikos, Y., Von Tengg-Kobligk, H., 2013a. A longitudinal study of Type-B aortic dissection and endovascular repair scenarios: Computational analyses. Med Eng Phys 35, 1321–1330. https://doi.org/10.1016/j.medengphy.2013.02.006

Chen, D., Müller-Eschner, M., von Tengg-Kobligk, H., Barber, D., Böckler, D., Hose, R., Ventikos, Y., 2013b. A patient-specific study of type-B aortic dissection: Evaluation of true-false lumen blood exchange. Biomed Eng Online 12, 1–16. https://doi.org/10.1186/1475-925X-12-65

Cosset, B., Boussel, L., Davila Serrano, E., Millon, A., Douek, P., Farhat, F., Sigovan, M., 2022. Hemodynamic Changes Before and After Endovascular Treatment of Type B Aortic Dissection by 4D Flow MRI. Front Cardiovasc Med 9. https://doi.org/10.3389/fcvm.2022.873144

De Beaufort, H.W.L., Coda, M., Conti, M., Van Bakel, T.M.J., Nauta, F.J.H., Lanzarone, E., Moll, F.L., Van Herwaarden, J.A., Auricchio, F., Trimarchi, S., 2017. Changes in aortic pulse wave velocity of four thoracic aortic stent grafts in an ex vivo porcine model. PLoS One 12. https://doi.org/10.1371/journal.pone.0186080

Di Achille, P., Tellides, G., Figueroa, C.A., Humphrey, J.D., 2014. A haemodynamic predictor of intraluminal thrombus formation in abdominal aortic aneurysms. Proceedings of the Royal Society A: Mathematical, Physical and Engineering Sciences 470. https://doi.org/10.1098/rspa.2014.0163

Dux-Santoy, L., Guala, A., Teixidó-Turà, G., Ruiz-Muñoz, A., Maldonado, G., Villalva, N., Galian, L., Valente, F., Gutiérrez, L., González-Alujas, T., Sao-Avilés, A., Johnson, K.M., Wieben, O., Huguet, M., García-Dorado, D., Evangelista, A., Rodríguez-Palomares, J.F., 2019. Increased rotational flow in the proximal aortic arch is associated with its dilation in bicuspid aortic valve disease. Eur Heart J Cardiovasc Imaging 20, 1407–1417. https://doi.org/10.1093/ehjci/jez046

Eidt, J.F., Vasquez, J., 2023. Changing Management of Type B Aortic Dissections. Methodist Debakey Cardiovasc J 19, 59–69. https://doi.org/10.14797/mdcvj.1171

Fielden, S.W., Fornwalt, B.K., Jerosch-Herold, M., Eisner, R.L., Stillman, A.E., Oshinski, J.N., 2008. A new method for the determination of aortic pulse wave velocity using cross-correlation on 2D PCMR velocity data. Journal of Magnetic Resonance Imaging 27, 1382–1387. https://doi.org/10.1002/jmri.21387

Gallo, D., Steinman, D.A., Bijari, P.B., Morbiducci, U., 2012. Helical flow in carotid bifurcation as surrogate marker of exposure to

13

disturbed shear. J Biomech 45, 2398–2404. https://doi.org/10.1016/j.jbiomech.2012.07.007

Gil-Sala, D., Guala, A., Garcia Reyes, M.E., Azancot, M.A., Dux-Santoy, L., Allegue Allegue, N., Teixido Turà, G., Goncalves Martins, G., Ruiz Muñoz, A., Constenla García, I., Evangelista, A., Tello Díaz, C., Ferreira González, I., Rodríguez-Palomares, J.F., Bellmunt, S., 2021. Geometric, Biomechanic and Haemodynamic Aortic Abnormalities Assessed by 4D Flow Cardiovascular Magnetic Resonance in Patients Treated by TEVAR Following Blunt Traumatic Thoracic Aortic Injury. European Journal of Vascular and Endovascular Surgery 62, 797–807. https://doi.org/10.1016/j.ejvs.2021.07.016

Girardin, L., Stokes, C., Thet, M.S., Oo, A.Y., Balabani, S., Díaz-Zuccarini, V., 2024. Patient-Specific Haemodynamic Analysis of Virtual Grafting Strategies in Type-B Aortic Dissection: Impact of Compliance Mismatch. Cardiovasc Eng Technol. https://doi.org/10.1007/s13239-024-00713-6

Guala, A., Gil Sala, D., Ruiz-Munoz, A., Garcia Reyes, M.E., Dux-Santoy, L., Teixido-Tura, G., Tello, C., Cinque, A., Valente, F., Lopez Sainz, A., Galian Gay, L., Ferreira, I., Evangelista, A., Bellmunt Montoya, S., Rodriguez Palomares, J.F., 2020. Patients with blunt traumatic thoracic aortic injury treated with TEVAR present increased flow dynamics alterations and pulse wave velocity: a 4D flow CMR study. Eur Heart J 41. https://doi.org/10.1093/ehjci/ehaa946.2351

Guala, A., Teixido-Tura, G., Dux-Santoy, L., Granato, C., Ruiz-Munõz, A., Valente, F., Galian-Gay, L., Gutiérrez, L., González-Alujas, T., Johnson, K.M., Wieben, O., Sao Avilés, A., Evangelista, A., Rodriguez-Palomares, J., 2019. Decreased rotational flow and circumferential wall shear stress as early markers of descending aorta dilation in Marfan syndrome: A 4D flow CMR study. Journal of Cardiovascular Magnetic Resonance 21. https://doi.org/10.1186/s12968-019-0572-1

Hori, D., Yuri, K., Kusadokoro, S., Shimizu, T., Kimura, N., Yamaguchi, A., 2020. Effect of endoprostheses on pulse wave velocity and its long-term outcomes after thoracic endovascular aortic repair. Gen Thorac Cardiovasc Surg 68, 1134–1141. https://doi.org/10.1007/s11748-020-01343-0

Jiang, X., Liu, Y., Zou, L., Chen, B., Jiang, J., Fu, W., Dong, Z., 2023. Long-Term Outcomes of Chronic Type B Aortic Dissection Treated by Thoracic Endovascular Aortic Repair. J Am Heart Assoc 12. https://doi.org/10.1161/JAHA.122.026914

Johnston, C.R., Lee, K., Flewitt, J., Moore, R., Dobson, G.M., Thornton, G.M., 2010. The

mechanical properties of endovascular stents: An in vitro assessment. Cardiovascular Engineering 10, 128–135. https://doi.org/10.1007/s10558-010-9097-9

Kousera, C.A., Wood, N.B., Seed, W.A., Torii, R., O'Regan, D., Xu, X.Y., 2013. A numerical study of aortic flow stability and comparison with in vivo flow measurements. J Biomech Eng 135. https://doi.org/10.1115/1.4023132

Lamata, P., Pitcher, A., Krittian, S., Nordsletten, D., Bissell, M.M., Cassar, T., Barker, A.J., Markl, M., Neubauer, S., Smith, N.P., 2014. Aortic relative pressure components derived from four-dimensional flow cardiovascular magnetic resonance. Magn Reson Med 72, 1162–1169. https://doi.org/10.1002/mrm.25015

Liu, Q., Jiang, P., Wu, J., Gao, B., Wang, S., 2019. The Morphological and Hemodynamic Characteristics of the Intraoperative Ruptured Aneurysm. Front Neurosci 13. https://doi.org/10.3389/fnins.2019.00233

Markl, M., Wallis, W., Brendecke, S., Simon, J., Frydrychowicz, A., Harloff, A., 2010. Estimation of global aortic pulse wave velocity by flow-sensitive 4D MRI. Magn Reson Med 63, 1575–1582. https://doi.org/10.1002/mrm.22353

Markl, M., Wallis, W., Harloff, A., 2011. Reproducibility of flow and wall shear stress analysis using flow-sensitive four-dimensional MRI. Journal of Magnetic Resonance Imaging 33, 988–994. https://doi.org/10.1002/jmri.22519

Midulla, M., Moreno, R., Negre-Salvayre, A., Beregi, J.P., Haulon, S., Loffroy, R., Dake, M., Rousseau, H., 2021. Impact of Thoracic Endografting on the Hemodynamics of the Native Aorta: Pre- and Postoperative Assessments of Wall Shear Stress and Vorticity Using Computational Fluid Dynamics. Journal of Endovascular Therapy 28, 63–69. https://doi.org/10.1177/1526602820959662

Morbiducci, U., Ponzini, R., Rizzo, G., Cadioli, M., Esposito, A., De Cobelli, F., Del Maschio, A., Montevecchi, F.M., Redaelli, A., 2009. In vivo quantification of helical blood flow in human aorta by time-Resolved three-dimensional cine phase contrast magnetic resonance imaging. Ann Biomed Eng 37, 516–531. https://doi.org/10.1007/s10439-008-9609-6

Morrison, T.M., Choi, G., Zarins, C.K., Taylor, C.A., 2009. Circumferential and longitudinal cyclic strain of the human thoracic aorta: Age-related changes. J Vasc Surg 49, 1029–1036. https://doi.org/10.1016/j.jvs.2008.11.056

Nauta, F.J.H., Lau, K.D., Arthurs, C.J., Eagle, K.A., Williams, D.M., Trimarchi, S., Patel, H.J., Figueroa, C.A., 2017. Computational Fluid Dynamics and Aortic Thrombus Formation Following Thoracic Endovascular Aortic Repair.

Annals of Thoracic Surgery 103, 1914–1921. https://doi.org/10.1016/j.athoracsur.2016.09.067

Nguyen, L.A., Houriez-Gombaud-Saintonge, S., Puymirat, E., Gencer, U., Dietenbeck, T., Bouaou, K., De Cesare, A., Bollache, E., Mousseaux, E., Kachenoura, N., Soulat, G., 2023. Aortic Stiffness Measured from Either 2D/4D Flow and Cine MRI or Applanation Tonometry in Coronary Artery Disease: A Case–Control Study. J Clin Med 12. https://doi.org/10.3390/jcm12113643

Nienaber, C.A., Kische, S., Rousseau, H., Eggebrecht, H., Rehders, T.C., Kundt, G., Glass, A., Scheinert, D., Czerny, M., Kleinfeldt, T., Zipfel, B., Labrousse, L., Fattori, R., Ince, H., 2013. Endovascular repair of type B aortic dissection: Long-term results of the randomized investigation of stent grafts in aortic dissection trial. Circ Cardiovasc Interv 6, 407–416. https://doi.org/10.1161/CIRCINTERVENTIONS.113.000463

Peacock, J., Jones, T., Tock, C., Lutz, R., 1998. The onset of turbulence in physiological pulsatile flow in a straight tube. Exp Fluids 24, 1–9. https://doi.org/10.1007/s003480050144

Pons, R., Guala, A., Rodríguez-Palomares, J.F., Cajas, J.C., Dux-Santoy, L., Teixidó-Tura, G., Molins, J.J., Vázquez, M., Evangelista, A., Martorell, J., 2020. Fluid–structure interaction simulations outperform computational fluid dynamics in the description of thoracic aorta haemodynamics and in the differentiation of progressive dilation in Marfan syndrome patients. R Soc Open Sci 7. https://doi.org/10.1098/rsos.191752

Reymond, P., Merenda, F., Perren, F., Rü, D., Stergiopulos, N., 2009. First published May 8, 2009; Downloaded from journals.physiology.org/journal/ajpheart at Univ Col London. Am J Physiol Heart Circ Physiol 297, 208–222. https://doi.org/10.1152/ajpheart.00037.2009.-A

Rovas, G., Bikia, V., Stergiopulos, N., 2023. Design and computational optimization of compliance-matching aortic grafts. Front Bioeng Biotechnol 11. https://doi.org/10.3389/fbioe.2023.1179174

Singh, S., Nassiri, N., Vallabhajosyula, P., 2021. All type B aortic dissections should undergo thoracic endovascular aneurysm repair. JTCVS Tech 9, 17–24. https://doi.org/10.1016/j.xjtc.2021.05.029

Stokes, C., Ahmed, D., Lind, N., Haupt, F., Becker, D., Hamilton, J., Muthurangu, V., von Tengg-Kobligk, H., Papadakis, G., Balabani, S., Díaz-Zuccarini, V., 2023a. Aneurysmal growth in type-B aortic dissection: assessing the impact of patient-specific inlet conditions on key

haemodynamic indices. J R Soc Interface 20. https://doi.org/10.1098/rsif.2023.0281

Stokes, C., Bonfanti, M., Li, Z., Xiong, J., Chen, D., Balabani, S., Díaz-Zuccarini, V., 2021. A novel MRI-based data fusion methodology for efficient, personalised, compliant simulations of aortic haemodynamics. J Biomech 129, 110793. https://doi.org/10.1016/j.jbiomech.2021.110793

Stokes, C., Haupt, F., Becker, D., Muthurangu, V., von Tengg-Kobligk, H., Balabani, S., Díaz-Zuccarini, V., 2023b. The Influence of Minor Aortic Branches in Patient-Specific Flow Simulations of Type-B Aortic Dissection. Ann Biomed Eng. https://doi.org/10.1007/s10439-023-03175-4

Sultan, S., Acharya, Y., Soliman, O., Parodi, J.C., Hynes, N., 2022. TEVAR and EVAR, the unknown knowns of the cardiovascular hemodynamics; and the immediate and long-term consequences of fabric material on major adverse clinical outcome. Front Surg 9, 1–8. https://doi.org/10.3389/fsurg.2022.940304

Tadros, R.O., Tang, G.H.L., Barnes, H.J., Mousavi, I., Kovacic, J.C., Faries, P., Olin, J.W., Marin, M.L., Adams, D.H., 2019. Optimal Treatment of Uncomplicated Type B Aortic Dissection: JACC Review Topic of the Week. J Am Coll Cardiol 74, 1494–1504. https://doi.org/10.1016/j.jacc.2019.07.063

Takahashi, K., Sekine, T., Ando, T., Ishii, Y., Kumita, S., 2022. Utility of 4D Flow MRI in Thoracic Aortic Diseases: A Literature Review of Clinical Applications and Current Evidence. Magnetic Resonance in Medical Sciences 21, 327–339. https://doi.org/10.2463/mrms.rev.2021-0046

Tomaiuolo, G., Carciati, A., Caserta, S., Guido, S., 2016. Blood linear viscoelasticity by small amplitude oscillatory flow. Rheol Acta 55, 485–495. https://doi.org/10.1007/s00397-015-0894-3

Trahanas, J.M., Jarral, O.A., Long, C., Hughes, G.C., 2022. Management of chronic type B aortic dissection. Vessel Plus 6. https://doi.org/10.20517/2574-1209.2021.125

Tremblay, D., Zigras, T., Cartier, R., Leduc, L., Butany, J., Mongrain, R., Leask, R.L., 2009. A Comparison of Mechanical Properties of Materials Used in Aortic Arch Reconstruction. Annals of Thoracic Surgery 88, 1484–1491. https://doi.org/10.1016/j.athoracsur.2009.07.023

Uchida, T., Sadahiro, M., 2018. Thoracic Endovascular Aortic Repair for Acute Aortic Dissection. Ann Vasc Dis 11, 464–472. https://doi.org/10.3400/avd.ra.18-00127

Valencia-Hernández, C.A., Lindbohm, J. V., Shipley, M.J., Wilkinson, I.B., McEniery, C.M., Ahmadi-Abhari, S., Singh-Manoux, A., Kivimäki, M., Brunner, E.J., 2022. Aortic Pulse Wave Velocity as Adjunct Risk Marker for Assessing

Cardiovascular Disease Risk: Prospective Study. Hypertension 79, 836–843. https://doi.org/10.1161/HYPERTENSIONAHA.121.17589

Van Bakel, T.M.J., Arthurs, C.J., Nauta, F.J.H., Eagle, K.A., Van Herwaarden, J.A., Moll, F.L., Trimarchi, S., Patel, H.J., Figueroa, C.A., 2019. Cardiac remodelling following thoracic endovascular aortic repair for descending aortic aneurysms. European Journal of Cardio-thoracic Surgery 55, 1061–1070. https://doi.org/10.1093/ejcts/ezy399

Wang, X., Carpenter, H.J., Ghayesh, M.H., Kotousov, A., Zander, A.C., Amabili, M., Psaltis, P.J., 2023. A review on the biomechanical behaviour of the aorta. J Mech Behav Biomed Mater 144, 105922. https://doi.org/10.1016/j.jmbbm.2023.105922

Wee, I., Ong, C.W., Syn, N., Choong, A., 2018. Computational Fluid Dynamics and Aortic Dissections: Panacea or Panic? Vascular and Endovascular Review 1, 27–29. https://doi.org/10.15420/ver.2018.8.2

Wentland, A.L., Grist, T.M., Wieben, O., 2014. Review of MRI-based measurements of pulse wave velocity: a biomarker of arterial stiffness. Cardiovasc Diagn Ther 4, 193–206. https://doi.org/10.3978/j.issn.2223-3652.2014.03.04

Westerhof, N., Lankhaar, J.W., Westerhof, B.E., 2009. The arterial windkessel. Med Biol Eng Comput. https://doi.org/10.1007/s11517-008-0359-2

Williams, M.L., de Boer, M., Hwang, B., Wilson, B., Brookes, J., McNamara, N., Tian, D.H., Shiraev, T., Preventza, O., 2022. Thoracic endovascular repair of chronic type B aortic dissection: A systematic review. Ann Cardiothorac Surg 11, 1–15. https://doi.org/10.21037/ACS-2021-TAES-25

Yuan, X., Mitsis, A., Ghonem, M., Iakovakis, I., Nienaber, C.A., 2018. Conservative management versus endovascular or open surgery in the spectrum of type B aortic dissection. J Vis Surg 4, 59–59. https://doi.org/10.21037/jovs.2018.02.15

Zhu, Y., Mirsadraee, S., Asimakopoulos, G., Gambaro, A., Rosendahl, U., Pepper, J., Xu, X.Y., 2021. Association of hemodynamic factors and progressive aortic dilatation following type A aortic dissection surgical repair. Sci Rep 11. https://doi.org/10.1038/s41598-021-91079-5